P13 Analyzing Radar Observed Mesocyclone Using Vortex-Flow-Dependent Background Covariance

Qin Xu[1]*, Li Wei[2] and Kang Nai[2]

[1]NOAA/National Severe Storms Laboratory, Norman, Oklahoma
[2]Cooperative Institute for Mesoscale Meteorological Studies, University of Oklahoma

1. Introduction

Detecting and tracking mesocyclones from Doppler radial-velocity fields are very important for tornado-related severe weather warning operations, but the involved tasks often encounter enormous difficulties especially when mesocyclones are poorly resolved in the far radial ranges or confused with other signatures or data artifacts (such as noisy or improperly dealiased velocities) in radial-velocity fields. To overcome the encounter difficulties, various automated mesocyclone detection methods and algorithms have been developed by many investigators (Stumpf et al. 1998; Smith and Elmore 2004; Liu et al. 2007; Newman et al. 2013; Miller et al. 2013). These methods rely on the assumption that a mesocyclone is behaving as a Rankine vortex and identify it as an object with no attempt to diagnose the detailed vortex wind field. To diagnose the full storm wind field, Gao et al. (2013) adapted a real-time three-dimensional variational data assimilation (3DVar) system and showed the value of the wind field assimilated from multiple Doppler radar data. This 3DVar system compares favorably to the methods described above with regards to identifying storm-scale mid-level circulations, but the circulation may not be fully resolved due to the isotropic univariant background covariance used for each velocity component in the cost-function. It is possible to improve the mesocyclone wind analysis by formulating the background covariance with vortex-flow dependences in a moving frame following the mesocyclone. This approach is explored in this paper and implemented as a new addition to the radar wind analysis system (RWAS, Xu et al. 2009).

The RWAS contains a radial-velocity data quality control (QC) package to preprocess the raw data for the vector wind analysis. This QC package is recently upgraded with the newly developed algorithms to detect and correct aliased velocities over small-scale areas threatened by intense mesocyclones and their generated tornados (Xu et al. 2013). The vector wind analysis in the RWAS uses the multivariant background covariance formulated for radar radial and tangential velocity components to retrieve the horizontal vector wind field from radar observed radial velocities (Xu et al. 2006), while the background error covariance is estimated statistically from the differences between the radar observed and background radial velocities (Xu et al. 2007). The early RWAS was designed to retrieve the vector wind field on each individual tilt of each radar volumetric scan in real time, and the retrieved wind field has been used to drive high-resolution emergency response dispersion models for homeland security applications (Fast et al. 2008). To monitor hazardous wind conditions at high spatial and temporal resolutions, the vector wind analysis in the RWAS has been upgraded to retrieve the real-time vector wind field in a mesoscale domain by using not only radial velocities scanned from operational WSR-88D radars but also Oklahoma Mesonet wind data. The analyzed vector wind field will be used as the background field in this paper, and a new variational method will be developed with vortex-flow-dependent background error covariance functions in an incremental form with respect to this background field for analyzing radar observed mesocyclone in a vortex-following coordinate system. In the next section, we will review the vector wind analysis in the RWAS and show its inability to resolve tornadic mesocyclones. We will then present the new variational method with vortex-flow-dependent background error covariance functions and show its satisfactory performance in resolving the tornadic mesocyclone in section 3. Conclusions follow in section 4.

2. Vector wind analysis in RWAS

The vector wind analysis in the RWAS performs three steps:

(a) A vertical profile of VAD vector wind $\mathbf{v} = (u, v)$ from dealiased radial velocities is produced for each radar, and then the VAD winds are assimilated at each vertical level (every 50 m above the radar site) with $\sigma_b \geq \sigma_o$ and $L = 150$ km, where σ_b^2 (or σ_o^2) denotes the background (or observation) error variance and L the background error de-correlation length. The nearest forecasts from the NCEP operational rapid refresh (RAP) model are interpolated in time and space to the wind analysis grid to generate the background wind field. The analysis in this step can be also performed with zero background wind field.

(b) The wind field produced by the previous step is used as a new background to assimilate the Oklahoma Mesonet wind data (at $z = 10$ m) with $\sigma_b \geq \sigma_o$ and $L = 60$ km.

(c) The wind field from the above step-2 is used as a new background to assimilate super-observations generated by combining dealiased radar velocities in three batches with the resolution coarsened to 13, 21 and 30 km (in both the radial and azimuthal directions), respectively, over the near radial ranges ($r \leq 40$ km), middle radial ranges (40 km $< r \leq$ 80 km) and far radial ranges ($r > 80$ km) from each radar. The observation error is estimated (between 1 m s$^{-1} \leq \sigma_o \leq 2$ m s^{-1}) for each super-observation based on the number of dealiased radial velocities within the area represented by that super-observation.

In the above three-step analysis, the 2D statistical interpolation of Xu et al. (2006) is extended to a 3D version to assimilate super-observations from each batch (serially from the far range to the near range) and update the background wind field. After each update, σ_b^2 is re-estimated for the next update by subtracting the spatially averaged super-observation

* Corresponding author address: Qin Xu, National Severe Storms Laboratory, 120 David L. Boren Blvd., Norman, OK 73072-7326; E-mail: Qin.Xu@noaa.gov

variance σ_o^2 from the spatially averaged variance of super-observation minus background. The 3D background error auto-correlation function between the radial winds v_{r1} at ($\mathbf{x}_1$, z_1) and v_{r2} at ($\mathbf{x}_2$, z_2) and the cross-correlation function between the radial wind v_{r1} at ($\mathbf{x}_1$, z_1) and tangential wind v_{t2} at ($\mathbf{x}_2$, z_2) are formulated by modifying (2.5a, b) of Xu et al. (2006) into

$$C(v_{r1}, v_{r2}) = \cos\Delta\beta \exp[-(|\Delta\mathbf{x}|^2/L^2 + \Delta z^2/D^2 + |\Delta\mathbf{v}|^2/V^2)/2],$$
$$C(v_{r1}, v_{t2}) = \sin\Delta\beta \exp[-(|\Delta\mathbf{x}|^2/L^2 + \Delta z^2/D^2 + |\Delta\mathbf{v}|^2/V^2)/2],$$

where $\Delta\beta = \beta_2 - \beta_1$, β_1 (or β_2) is the azimuthal angle of point $\mathbf{x}_1$ (or $\mathbf{x}_2$) viewed from the radar, $\Delta\mathbf{x} = \mathbf{x}_2 - \mathbf{x}_1$ is the horizontal distance and $\Delta z = z_2 - z_1$ is the vertical distance between the two points, D is the de-correlation depth, $\Delta\mathbf{v} = \mathbf{v}(z_2) - \mathbf{v}(z_1)$ is the increment of the VAD wind $\mathbf{v} = (u, v)$ over Δz, and V scales the de-correlation enhanced by $|\Delta\mathbf{v}|$. The background error de-correlation length L (or depth D) is set to 25 (or 2), 18 (or 1) and 11 (or 0.3) km for the three serial updates, respectively. As a shear-dependent term, $|\Delta\mathbf{v}|^2/V^2$ is introduced (with V = 1 m s^{-1}) in the above correlation functions to reduce the vertical correlation adaptively across a strong vertical-shear layer. This term improves the wind analysis especially when the flow field contains a strong vertical-shear layer that is often observed in winter ice storms. The RWAS can capture sharp wind reversals in the vertical as well as strong horizontal shears associated with mesoscale fronts (see Figs. 3–5 of Xu et al. 2009).

Figure 1a shows the background wind field from the operational RAP forecast and Fig. 1b shows the analyzed wind field produced by the RWAS using radial velocities scanned from five operational WSR-88D radars plus Oklahoma Mesonet wind data around 221123 UTC for the tornadic storm on 24 May 2011. In comparison with the background winds in Fig. 1a, the analyzed winds in Fig. 1b are adjusted moderately toward radar observed radial winds mainly and only in areas covered by radar radial-velocity observations. As shown in Fig. 1b, the analyzed winds are deflected and curved around the tornado-generating mesocyclone (marked by the small yellow circle) but still too smooth to resolve the mesocyclone winds.

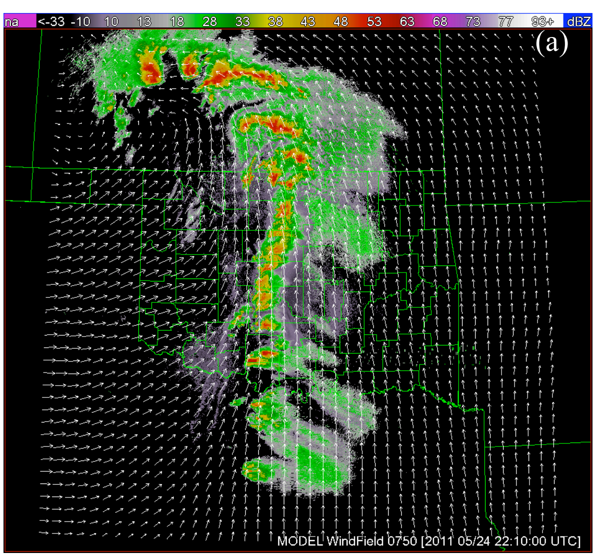

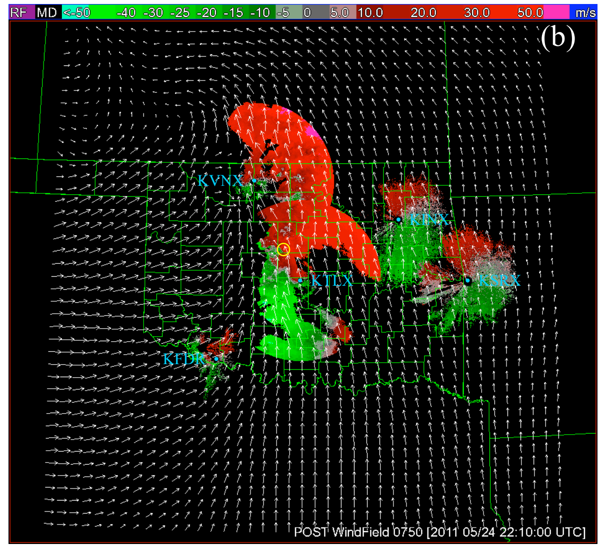

Fig. 1. (a) RAP forecast wind field at z = 0.75 km superimposed on the reflectivity image from five radars for the tornadic storm at 221123 UTC 5/24/2011. (b) RWAS analyzed wind field at z = 0.75 km superimposed on the dealiased radial-velocity images at 4.0° tilt from KVNX and KTLX radars, 0.9° tilt from KFDR radar, and 0.5° tilt from KINX and KSRX radars. Each radar site is marked by a blue dot with the radar name in panel (b). The small yellow circle in panel (b) marks the tornadic mesocyclone.

3. Vortex wind analysis

To resolve the mesocyclone, an additional step is designed and performed to analyze the vortex wind field around the mesocyclone from the dealiased radial velocities observed by the KTLX or KFDR radar (without combining into super-observations) in a 20×20 km^2 nested domain co-centered with the vortex in a moving frame following the mesocyclone on each tilt of radar scan. The mesocyclone area is identified as a by-product of the velocity dealiasing (see Appendix of Xu et al. 2013). The vortex center is estimated on each tilt of radar scan by applying the following two-step algorithm to the radial-velocity innovations (that is, $v_r^i = v_r^o - v_r^b$ where v_r^o is the dealiased observation and v_r^b is the background radial-velocity) in the mesocyclone area:

I. Find $v_{r\max}$ and $v_{r\min}$ with $\varphi_{\max} > \varphi_{\min}$ along each range circle over the sector data area of 20 km arc length and 20 km radial range that covers the mesocyclone, where $v_{r\max}$ (or $v_{r\min}$) is the maximum (or minimum) v_r^i and $\varphi_{\max}$ (or $\varphi_{\min}$) is the azimuthal angle of $v_{r\max}$ (or $v_{r\min}$) data point. Denote by r_m the radial range at which $(v_{r\max} - v_{r\min})/(\varphi_{\max} - \varphi_{\min})$ is largest and by φ_m the value of $(\varphi_{\max} + \varphi_{\min})/2$ on the rang circle of $r = r_m$. The vortex center location is then first estimated by (r_m, φ_m) in the radar coordinates, and the interpolated value of v_r^i at (r_m, φ_m), denoted by $v_{r\,m}^i$, is the radial component of the moving velocity of the estimated vortex center relative to the background flow.

II. Find and denote by $(r_j, \varphi_j) = (j\Delta r, \varphi_j)$ the location where $v_r^i - v_{r\,m}^i$ changes sign (from negative to positive as φ increases) between two adjacent beams along the j-th range circle in the data window of 11 beams and 11 range gates centered at

(r_m, φ_m), where Δr (= 250 m) is the range gate spacing. Denote by Δv_{rj} (> 0) the increment of v_r^{i} associated with the sign change of $v_r^{\mathrm{i}} - v_{r\,m}^{\mathrm{i}}$ at (r_j, φ_j). The final estimate of the vortex center location is given by

$$(r_c, \varphi_c) = \textstyle\sum_j (r_j, \varphi_j)(\Delta v_{rj}/\Delta l_j)^2 / \sum (\Delta v_{rj}/\Delta l_j)^2,$$

where $\sum_j$ denotes the summation over j for the five range circles that have the first five largest values of Δv_{rj}, and $(\Delta l_j)^2 = (r_j - r_m)^2 + r_j^2(\varphi_j - \varphi_m)^2$.

The RWAS analyzed wind field (Fig. 1b) is projected onto the 20×20 km^2 nested domain on each tilt to provide the background wind field for the vortex wind analysis. The control variables used for the analysis are the streamfunction, Ψ, and velocity potential, χ, defined by

$$\Delta u = -\partial_y \Psi + \partial_x \chi \ \text{ and } \ \Delta v = \partial_x \Psi + \partial_y \chi, \tag{1}$$

where $(\Delta u, \Delta v)$ is the horizontal-velocity increment with respect to the projected background wind field in the moving frame. The radial-velocity increment, Δv_r, in the moving frame is then related to (Ψ, χ) by

$$\begin{aligned}\Delta v_r &= (\Delta u \sin\varphi + \Delta v \cos\varphi)\cos\theta \\ &= [(-\partial_y \Psi + \partial_x \chi)\sin\varphi + (\partial_x \Psi + \partial_y \chi)\cos\varphi]\cos\theta,\end{aligned} \tag{2}$$

where φ is the radar beam azimuthal angle (positive for clockwise rotation from the y-coordinate pointing to the north) and θ is the radar beam slope angle at the data point. The projection of the vertical velocity w is neglected in (2) since θ is small and w is not analyzed.

The cost-function has the following incremental form:

$$J = \Delta\mathbf{a}^{\mathrm{T}}\mathbf{B}^{-1}\Delta\mathbf{a}/2 \ + (\mathbf{H}\Delta\mathbf{a} - \mathbf{d})^{\mathrm{T}}\mathbf{R}^{-1}(\mathbf{H}\Delta\mathbf{a} - \mathbf{d})/2, \tag{3}$$

where $\Delta\mathbf{a}$ is the state vector of (Ψ, χ), $\mathbf{B}$ is the background error covariance matrix, $\mathbf{R}$ is the observation error covariance matrix, $\mathbf{H}$ is the observation operator expressed in (2), and $\mathbf{d}$ is the innovation vector in the moving frame following the mesocyclone vortex center, that is, the state vector of $v_r^{\mathrm{o}} - v_r^{\mathrm{b}} - v_{r\,m}^{\mathrm{i}}$ where v_r^{o} is the dealiased radial-velocity observation, v_r^{b} is the background radial velocity and $v_{r\,m}^{\mathrm{i}}$ is the radial component of the vortex center moving velocity relative to the background flow (estimated in step-I). The observation errors are assumed to be uncorrelated between different points, so $\mathbf{R} = \sigma_{\mathrm{o}}^2\mathbf{I}$, where σ_{o}^2 is the observation error variance and $\mathbf{I}$ is the identity in the observation space.

The background error covariance matrix is constructed by the following vortex-flow-dependent covariance functions

$$B_{yy}(\mathbf{x}_i, \mathbf{x}_j) = \sigma_\psi^2 C(\rho_{ij}, \phi_{ij}),$$
$$B_{cc}(\mathbf{x}_i, \mathbf{x}_j) = \sigma_\chi^2 C(\rho_{ij}, \phi_{ij}),$$

where

$$C(\rho_{ij}, \phi_{ij}) = \exp[-(\rho_{ij}^2/R^2 + \phi_{ij}^2/\Phi^2)/2] = C_1(\rho_{ij})C_2(\phi_{ij}),$$

$|\mathbf{x}| = (x^2 + y^2)^{1/2}$, $(\ )_i$ [or $(\ )_j$] denotes the value of $(\ )$ at the point i (or j), σ_ψ^2 (or σ_χ^2) is the background error variance for Ψ (or χ), $\rho_{ij} = \rho_i - \rho_j$, $\phi_{ij} = \phi_i - \phi_j$, R (or Φ) is the radial (or azimuthal) de-correlation length in ρ (or ϕ), (ρ, ϕ) are related to (x, y) in the local coordinate system co-centered with the vortex by

$$\rho = \ln(|\mathbf{x}|/R_{\mathrm{M}}) \text{ for } |\mathbf{x}_i| \le R_{\mathrm{M}}$$
$$\rho = |\mathbf{x}_i|/R_{\mathrm{M}} - 1 \text{ for } |\mathbf{x}_i| > R_{\mathrm{M}},$$
$$\phi = \tan^{-1}(y/x),$$

and R_M is the estimated radius of maximum tangential velocity of the vortex (see Appendix of Xu et al. 2013). The estimated value is R_M = 3 km for the mesocyclone scanned by the KFDR and KTLX radars on 24 May 2011. By setting, R = 1.0 and Φ = 1 in arc (or 180°/π), $C(\rho_{ij}, \phi_{ij})$ is plotted in Fig. 2.

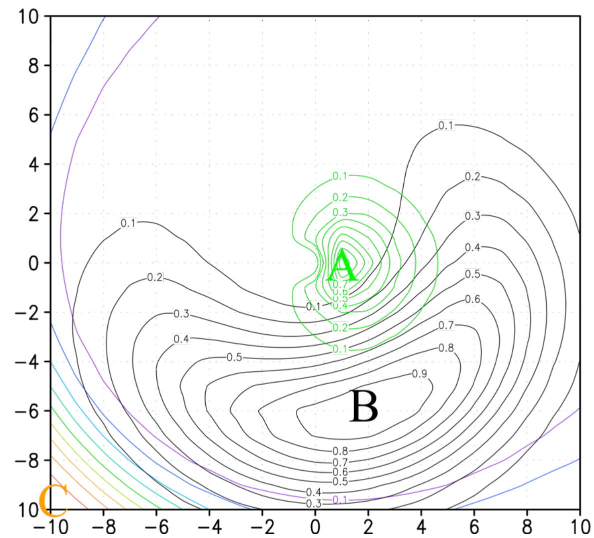

Fig. 2. $C(\mathbf{x}_i, \mathbf{x}_j)$ plotted as functions of $\mathbf{x}_i$ by the green, black and yellow contours for $\mathbf{x}_j$ fixed at A, B & C, respectively, where R = 1, Φ = 180°/π and R_{M} = 3 km.

By using the Fourier transformation in (ρ, ϕ) and the convolution theorem, we obtain

$$\begin{aligned}C(\rho_{ij}, \phi_{ij}) &= \textstyle\int P_1(\rho_i - \rho_s)P_1(\rho_s - \rho_j)d\rho_s \int P_2(\phi_i - \phi_s)P_2(\phi_s - \phi_j)d\phi_s \\ &\approx \textstyle\sum_s P_1(\rho_{is})P_2(\phi_{is})P_1(\rho_{sj})P_2(\phi_{sj})\Delta r\Delta\phi = \sum_s P_{is}P_{sj},\end{aligned} \tag{4}$$

where
$$P_1(\rho_{is}) = (2/\pi)^{1/4}R^{-1/2}\exp(-\rho_{is}^2/R^2),$$
$$P_2(\phi_{is}) = (2/\pi)^{1/4}F^{-1/2}\textstyle\sum_n \exp[-(\phi_{is} - 2n\pi)^2/F^2]$$
$$\approx (2/\pi)^{1/4}F^{-1/2}\exp(-\phi_{is}^2/F^2),$$
$$P_{is} = P_1(\rho_{is})P_2(\phi_{is})(\Delta\rho\Delta\phi)^{1/2},$$

$\Delta\rho$ (or $\Delta\phi$) is the ρ (or ϕ) grid resolution for the discrete integration in (4), and the (ρ, ϕ)-grid covers the data area with an extended margin of $2R$ on each side of the ρ-grid. The matrix form of (4) is $\mathbf{C} = \mathbf{P}\mathbf{P}^{\mathrm{T}}$ where $\mathbf{C} = \{C_{ij}\}$, $\mathbf{P} = \{P_{is}\}$ and $\mathbf{P}^{\mathrm{T}} = \{P_{sj}\}$ is the transpose of $\mathbf{P}$. This gives $(\sigma_\chi\mathbf{P}, \sigma_\psi\mathbf{P})^{\mathrm{diag}}(\sigma_\chi\mathbf{P}^{\mathrm{T}}, \sigma_\psi\mathbf{P}^{\mathrm{T}})^{\mathrm{diag}} = (\sigma_\chi^2\mathbf{P}\mathbf{P}^{\mathrm{T}}, \sigma_\psi^2\mathbf{P}\mathbf{P}^{\mathrm{T}})^{\mathrm{diag}} = (\sigma_\chi^2\mathbf{C}, \sigma_\psi^2\mathbf{C})^{\mathrm{diag}} = \mathbf{B}$, so $\mathbf{B}^{1/2} = (\sigma_\chi\mathbf{P}, \sigma_\psi\mathbf{P})^{\mathrm{diag}}$ is the root square of $\mathbf{B}$ satisfying $\mathbf{B}^{1/2}\mathbf{B}^{\mathrm{T}/2} = \mathbf{B}$. Substituting $\Delta\mathbf{a} = \mathbf{B}^{1/2}\mathbf{a}'$ with $\mathbf{R} = \sigma_{\mathrm{o}}^2\mathbf{I}$ into (3) gives

$$J = |\mathbf{a}'|^2/2 + |\mathbf{H}'\mathbf{a}' - \mathbf{d}|^2/(2\sigma_o^2), \quad (5)$$

where **H**' is the radial-velocity observation operator expressed by the transformed control vector **a**' and the detailed formulation of **H**' is omitted here. Since the nested domain is small, the control vector **a**' is constructed on a 27x18 uniform (ρ, ϕ)-grid with $\Delta\rho = R/3 = 1/3$ to cover the range of $-9 \le \rho \le 17$ and $\Delta\phi = \Phi\pi/9 = \pi/9$ to cover the entire range of $-\pi < \phi \le \pi$. In this case, although the observation space dimension can exceed 10^3, the control-vector space dimension is merely 25x18 = 450, so the singular-value decomposition of **H**' can be computed efficiently to give $\mathbf{H}' = \mathbf{U}\mathbf{\Lambda}\mathbf{V}^T$, where $\mathbf{\Lambda}$ is a diagonal matrix composed of the singular values of **H**', and **U** and **V** are the orthogonal matrices composed of the left and right singular vectors of **H**', respectively. Substituting $\mathbf{H}' = \mathbf{U}\mathbf{\Lambda}\mathbf{V}^T$ into (5) gives the direct solution of $\nabla_{\mathbf{a}'}J = 0$ in the following concise form:

$$\mathbf{a}' = \mathbf{V}(\mathbf{I} + \mathbf{\Lambda}^2/\sigma_o^2)^{-1}\mathbf{\Lambda}\mathbf{U}\mathbf{d}/\sigma_o^2.$$

The state vector of (Ψ, X) for the incremental velocity field in (1) is then given by $\Delta\mathbf{a} = \mathbf{B}^{1/2}\mathbf{a}'$. The RMS error for the dealiased radial-velocity observations and their innovations is set to $\sigma_o = 4$ m s^{-1}, which is larger than that (1 m s$^{-1} \le \sigma_o \le 2$ m s^{-1}) estimated for the super-observations in section 2. The background RMS error for Ψ and X are set to $\sigma_\psi = f(|\mathbf{x}|)4\times10^4$ m^2 s^{-1} and $\sigma_\chi = f(|\mathbf{x}|)8\times10^3$ m^2 s^{-1}, respectively, to account for relatively large errors in the rotational part of the background wind field, where $f(|\mathbf{x}|) = 1$ for $|\mathbf{x}| \ge R_M$ and $f(|\mathbf{x}|) = (0.1 - 0.9|\mathbf{x}|/R_M)$ for $|\mathbf{x}| < R_M$ to account for the reduced background error (that is, the true velocity for zero background wind) toward the vortex center in the moving frame. From the above settings, the background RMS error for the rotational and divergent winds around the radius of maximum tangential velocity can be estimated by $\sqrt{2}\sigma_\psi/(RR_M) \approx 20$ m s^{-1} and $\sqrt{2}\sigma_\chi/(RR_M) \approx 4$ m s^{-1}, respectively, and these estimates are obtained by modifying (A.13) and (A14) of Xu et al (2010) to the (ρ, ϕ) coordinates.

With the above settings, the vortex wind field for the matured tornadic mesocyclone (marked by the small yellow circle in Fig. 1b) on 24 May 2011 is analyzed as an incremental wind field respect to the background wind field by using single-Doppler velocity observations from the KFDR or KTLX radar first and then by using dual-Doppler velocity observations from these two radars. The incremental vortex wind field obtained from the KFDR radial-velocity innovation data (that is, dealiased v_r^o from KFDR minus v_r^b and v_{rm}^i) on the 0.5° tilt (around $z = 4.28$ km) at 221015 UTC is plotted in Fig. 3a by the white arrows [changed to pink if $|(\Delta u, \Delta v)| > 30$ m s^{-1}] superimposed on the KFDR radial-velocity innovation image in the nested domain, where $v_r^b = 28.5$ m s^{-1} at the vortex center and $v_{rm}^i = -4.1$ m s^{-1}. The estimated vortex center is at (r_c, φ_c) = (201.375 km, 38.2°) in the KFDR radar coordinates. The incremental vortex wind field obtained from the KTLX radial-velocity innovation data on the 4.0° tilt (around $z = 4.42$ km) at 221223 UTC is plotted in Fig. 3b by the white arrows superimposed on the KTLX radial-velocity innovation image in the nested domain, where $v_r^b = 16.0$ m s^{-1} at the vortex center and $v_{rm}^i = -2.6$ m s^{-1}. The estimated vortex center is at (r_c, φ_c) = (59.875 km, 331.5°) in the KTLX radar coordinates.

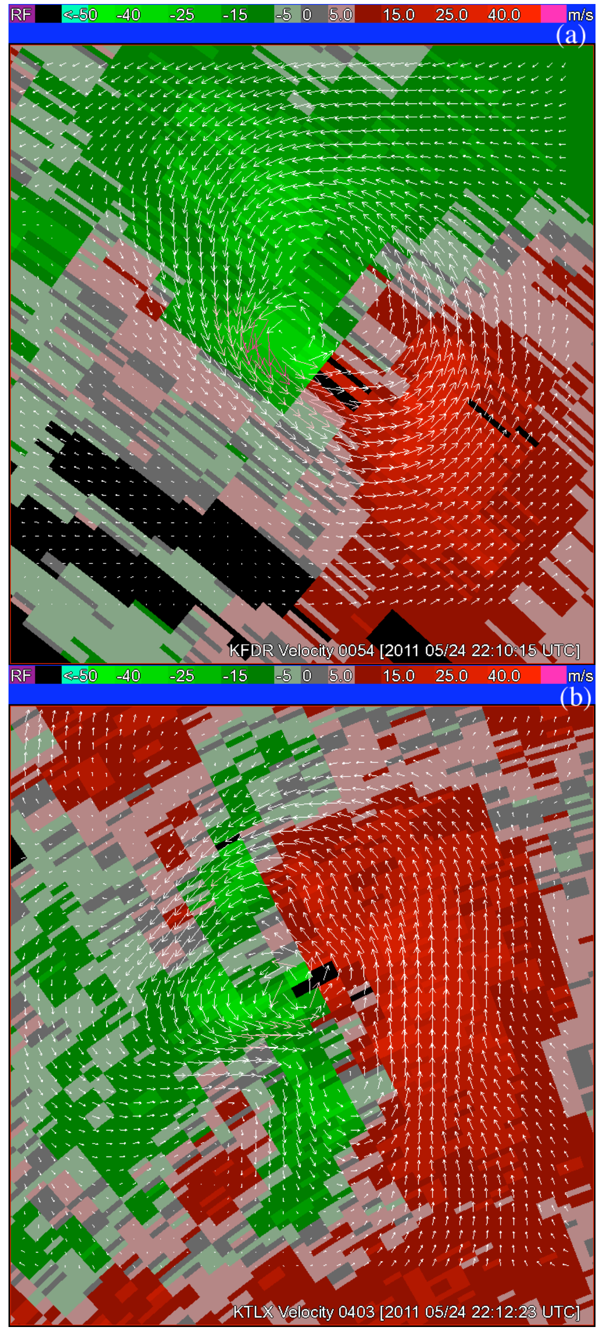

Fig. 3. (a) Analyzed incremental vortex winds plotted by white and pink (> 30 m/s) arrows superimposed on radial-velocity innovation (v_r^o - v_r^b - v_{rm}^i) image on the 0.5° tilt ($z \approx$ 4.28 km) from KFDR radar at 221015 UTC 5/24/2011. (b) As in (a) but on 4.0° tilt ($z \approx$ 4.42 km) from KTLX radar at 221223 UTC 5/24/2011.

As shown in Fig. 3a (or 3b), the analyzed vortex winds match the radial-velocity innovation image from the KFDR (or KTLX) radar quite closely. The maximum value of the analyzed vortex winds is 29.9 (or 26.4) m s^{-1} in Fig. 3a (or 3b), which is close to the absolute values of the positive and negative maxima [that is, 26.3 and -38.3 (or 24.7 and -27.1) m s^{-1}] of the observed radial-velocity innovations from the KFDR (or KTLX) radar. The spatially averaged RMS difference between the analyzed radial-velocity increments and observed radial-velocity innovations is 2.5 (or 3.5) m s^{-1} for the fields in Fig. 3a (or 3b). These RMS differences are smaller than the observation RMS error (σ_o = 4 m s^{-1}) and much smaller than the estimated background RMS error (20 m s^{-1}) for the rotational winds around the radius of maximum tangential velocity. These necessary conditions for the analysis optimality are satisfied by the above two single-Doppler analyses.

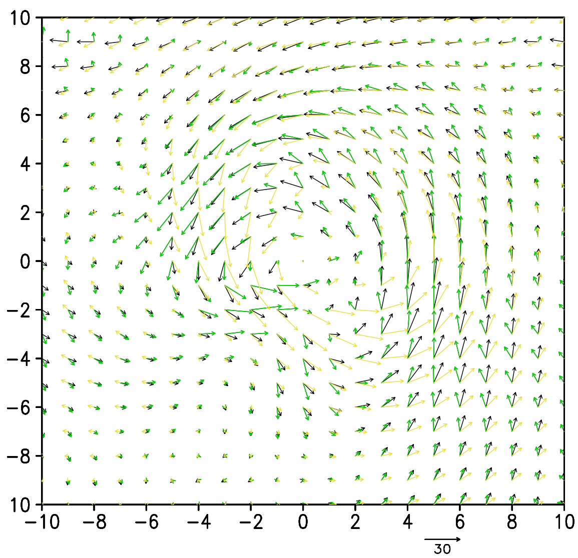

Fig. 4. Dual-Doppler analysis of vortex winds plotted by black arrows versus the single-Doppler analyses in Figs. 3a and 3b re-plotted by yellow and green arrows, respectively.

In Fig. 4, the dual-Doppler analysis of vortex winds is obtained from the KTLX radial-velocity innovation data on the 4.0^o tilt (around z = 4.42 km) and the KFDR radial-velocity innovation data on the 0.5^o tilt (around z = 4.28 km). This dual-Doppler analysis neglects the vertical variations of the true vertex winds between the two tilts (from $z \approx 4.42$ to 4.28 km) and assumes that the vortex center in the KFDR innovation data field is moved northeastward to the location of the vortex center in the KFLX innovation data field during the time period (of 128 s) from the KFDR-scan time (221015 UTC) to the KTLX-scan time (221223 UTC). As shown in Fig. 4, the dual-Doppler analyzed winds (black arrows) are mostly between the two single-Doppler analyzed winds (yellow and green arrows), especially in the two areas on the southeast and northwest sides of the vortex center where the two single-Doppler analyzed wind fields become significantly different. The spatially averaged RMS difference between the dual-Doppler analyzed wind field and the single-Doppler analyzed wind field from KFDR (or KTLX) radar is 7.3 (or 7.6) m s^{-1}. The spatially averaged RMS difference between the two single-Doppler analyzed wind fields is 10.9 m s^{-1}. The differences between the two single-Doppler analyzed wind fields could be caused by the variations of the true vortex winds with height (from z = 4.42 to 4.28 km) and time (from 221223 to 221223 UTC) in addition to the analysis errors.

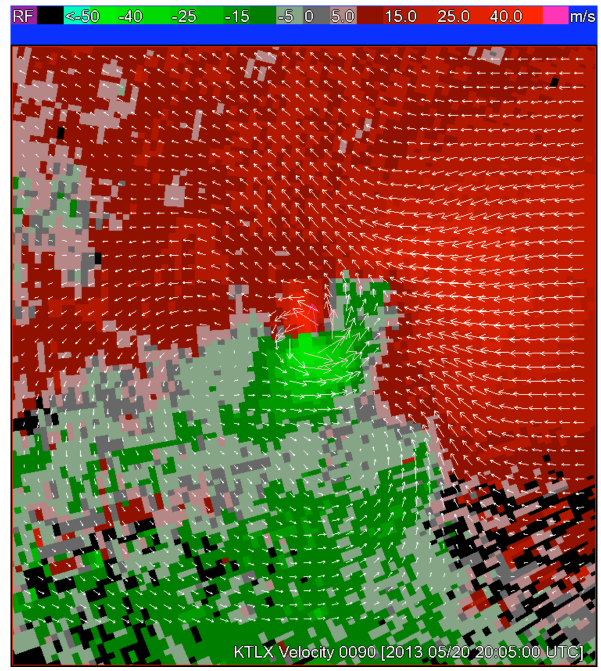

Fig. 5. As in Fig. 3b but for the analyzed vortex winds from KTLX innovation (v_r^o - $v_{r\,m}^{\,i}$) data on 0.9^o tilt ($z \approx 0.5$ km) for the Oklahoma Moore tornadic mesocyclone at 200500 UTC 5/20/2013.

The vortex wind can be also performed with zero background wind field. An example of this stand-alone application is shown in Fig. 5 for the tornadic storm that produced a strong mesocyclone and an EF5 tornado that struck the cities of Newcastle and Moore, Oklahoma in the afternoon (local time between 2:45pm and 3:35pm) on 20 May 2013. In particular, Fig. 5 shows the incremental vortex winds (white arrows for $|(\Delta u, \Delta v)| \le 30$ m s^{-1} and pink arrows for $|(\Delta u, \Delta v)| > 30$ m s^{-1}] obtained from the KTLX radial-velocity innovation data on the 0.9^o tilt (around z = 0.5 km) at 200500 UTC, where $v_{r\,m}^{\,i}$ = -4.2 m s^{-1}. The estimated vortex center is at (r_c, φ_c) = (28.875 km, 265.0^o) which is not far from the KTLX radar site, so the intense azimuthal shear of radial velocity around the vortex center and the strong radial divergence (or convergence) of radial velocity to north-northeast (or east-northeast) of the vortex center are resolved quite well by the KTLX radial-velocity innovation image in Fig. 5. The radial components of analyzed vortex winds match the KTLX radial-velocity innovations quite closely, especially around the vortex center and along the curved area of strong divergent (or convergent) winds to north-northeast (or east-northeast) of the vortex center, and their spatially averaged RMS difference is 2.5 m s^{-1}. The maximum value of the analyzed vortex winds is 37.6 m s^{-1} in Fig. 5, which is close to the absolute values of the positive and negative maxima [that is, 35.9 and -39.0 m s^{-1}] of the observed radial-velocity innovations from the KTLX radar.

4. Conclusions

In this paper, a vortex-flow-dependent correlation function is formulated and used to construct the background error covariance matrix for analyzing two-dimensional vortex winds from single-Doppler scan of a mesocyclone in a moving frame following the mesocyclone detected on each tilt of the radar scan. This vortex wind analysis method is computationally very efficient and has just been incorporated into our real-time radar wind analysis system (RWAS, Xu et al. 2009). The method has been successfully tested with several tornadic mesocyclones observed by operational radars (as exemplified in this paper) and will be applied to real-time radar observations of mesocyclones in the near future. The method can be extended to analyze three-dimensional vortex winds from either single-Doppler or multi-Doppler scans of mesocyclones, and this capability is under our current research development.

Acknowledgments

The research work was supported by the ONR Grant N000141010778 to the University of Oklahoma (OU). Funding was also provided to CIMMS by NOAA/Office of Oceanic and Atmospheric Research under NOAA-OU Cooperative Agreement #NA17RJ1227, U.S. Department of Commerce.

REFERENCES

Fast, J. D., R. K. Newsom, K. J. Allwine, Q. Xu, P. Zhang, J. Copeland, and J. Sun, 2008: An evaluation of two NEXRAD wind retrieval methedologies and their use in atmospheric dispersion models. *J. Appl. Meteor. & Climatology*, **47**, 2351–2371.

Gao, J., T. M. Smith, D. J. Stensrud, C. Fu, K. Calhoun, K. L. Mnaross, J. Brogden, V. Lakshmanan, Y. Wang, K. W. Thomas, K. Brewster, and M. Xue, 2013: A realtime weather-adaptive 3DVAR analysis system for severe weather detections and warnings. *Wea. Forecasting*, **28**, 727–745.

Liu, S., M. Xue, and Q. Xu, 2007: Using wavelet analysis to detect tornadoes from doppler radar radial-velocity observations. *J. Atmos. Oceanic Technol*., **24**, 344–359.

Miller, M. L., V. Lakshmanan, and T. M. Smith, 2013: An automated method for depicting mesocycone paths and intensities. *Wea. Forecasting*, **28**, 570–585.

Newman, J. F., V. Lakshmanan, P. L. Heinselman, M. B. Richman, and T. M. Smith, 2013: Range-correcting azimuthal shear in Doppler radar data. *Wea. Forecasting*, **28**, 194–211.

Smith, T. M., and K. L. Elmore, 2004: The use of radial velocity derivatives to diagnose rotation and divergence. Preprints, *11th Conf.on Aviation, Range and Aerospace*, Hyannis, MA, Amer. Meteor. Soc., P5.6.

Stumpf, G. J., A. Witt, E. D. Mitchell, P. L. Spencer, J. T. Johnson, M. D. Eilts, K. W. Thomas, and D. W. Burgess, 1998: The National Severe Storms Laboratory mesocyclone detection algorithm for the WSR-88D. *Wea. Forecasting*, **13**, 304–326.

Xu, Q., S. Liu, and M. Xue, 2006: Background error covariance functions for vector wind analyses using Doppler radar radial-velocity observations. *Quart. J. Roy. Meteor. Soc*., **132**, 2887–2904.

Xu, Q., K. Nai, and L. Wei, 2007: An innovation method for estimating radar radial-velocity observation error and background wind error covariances. *Quart. J. Roy. Meteor. Soc.*, **133**, 407–415.

Xu, Q., K. Nai, S. Liu, C. Karstens, T. Smith and Q. Zhao, 2013: Improved Doppler velocity dealiasing for radar data assimilation and storm-scale vortex detection. *Advances in Meteorology*, (in press).

Xu, Q., K. Nai, L. Wei, P. Zhang, Q. Zhao and P. R. Harasti, 2009: A real-time radar wind data quality control and analysis system for nowcast application. Extended Abstracts, *International Symposium on Nowcasting and Very Short Range Forecasting (WSN09)*, Whistler, British Columbia, Canada, WMO, 3.5. [Available online at http://www.nowcasting2009.ca/images/stories/Presentations/WSN09_Presentations.htm.]

Xu, Q., L. Wei, W. Gu, J. Gong, and Q. Zhao, 2010: A 3.5-dimensional variational method for Doppler radar data assimilation and its application to phased-array radar observations. *Advances in Meteorology*, Vol.**2010**, Article ID 797265, 14 pages, doi:10.1155/2010/797265.